Article

Multi-Modal Laser-Fabricated Nanocomposites with Non-Invasive Tracking Modality and Tuned Plasmonic Properties

Yury V. Ryabchikov [ID]

HiLASE Centre, Institute of Physics of the Czech Academy of Sciences, Za Radnicí 828,
25241 Dolní Břežany, Czech Republic; ryabchikov@fzu.cz; Tel.: +420-314-007-734

Abstract: Ultrapure composite nanostructures combining semiconductor and metallic elements as a result of ultrafast laser processing are important materials for applications in fields where high chemical purity is a crucial point. Such nanocrystals have already demonstrated prospects in plasmonic biosensing by detecting different analytes like dyes and bacteria. However, the structure of the nanocomposites, as well as the control of their properties, are still very challenging due to the significant lack of research in this area. In this paper, the synthesis of silicon–gold nanoparticles was performed using various approaches such as the direct ablation of (i) a gold target immersed in a colloidal solution of silicon nanoparticles and (ii) a silicon wafer immersed in a colloidal solution of plasmonic nanoparticles. The formed nanostructures combine both plasmonic (gold) and paramagnetic (silicon) modalities observed by absorbance and electron paramagnetic resonance spectroscopies, respectively. A significant narrowing of the size distributions of both types of two-element nanocrystals as compared to single-element ones is shown to be independent of the laser fluence. The impact of the laser ablation time on the chemical stability and the concentration of nanoparticles influencing their both optical properties and electrical conductivity was studied. The obtained results are important from a fundamental point of view for a better understanding of the laser-assisted synthesis of semiconductor–metallic nanocomposites and control of their properties for further applications.

Keywords: silicon nanoparticles; gold nanoparticles; composite nanoparticles; nanocomposites; laser ablation; pulsed laser ablation in liquids; plasmonic nanomaterials; multi-modal nanoparticles

1. Introduction

The fast development of the nanotechnology field over the last decades reveals new properties and applications of semiconductor and metallic nanomaterials in comparison with their bulk counterparts. In particular, new unique features (e.g., effective visible photoluminescence) were found in nanostructured silicon (nano-Si), considerably widening applications of silicon in photovoltaics [1–3], nanothermometry [4–6], or nanoscale electronic devices [7,8]. However, their most promising applications are related to the actively developing field of life science. Indeed, silicon nanostructures demonstrated their high efficiency in singlet oxygen generation [9–11], optical bioimaging [12,13], drug delivery [14,15] and cancer theranostics [16,17]. At the same time, plasmonic nanostructures show their efficiency not only in photocatalysis and clean energy but also in biosensing and therapeutic applications [18–20]. Moreover, recent advances in biomedical applications were also demonstrated using magnetic nanostructures [21–23].

Thus, several types of nanostructures are required for solving different tasks in the field of biomedicine such as drug delivery and the localization of malignant tumours, as well as diagnostic and therapeutic actions for them. It can provoke additional issues after administration of nanoparticles in living organisms, in particular, agglomeration of nanomaterials or toxicity effects. In order to avoid this, composite multi-functional nanoparticles (NPs) composed of different elements can serve as a new type of multi-modal nanoplatform

for biological applications [24–27]. However, their complex synthesis and toxicity effects due to the use of chemical precursors significantly restrict their bioapplications. In order to overcome the above-mentioned issues, an environmentally friendly "green" synthesis method based on ultrafast laser irradiation is widely used for the formation of single-element or bi-metallic nanostructures [28–33]. Recently, the possibility of manufacturing nanostructures by combining semiconductor and metallic elements in one nanoparticle was demonstrated [34–38]. Nevertheless, this field of laser–matter interaction, which is promising for biomedical applications, is still under development, providing the novelty of the research. It requires a deeper understanding of the processes that occur during the interaction between various elements and that will definitely depend on numerous experimental conditions.

In this work, colloidal solutions of chemically pure composite nanomaterials were synthesized by pulsed laser ablation in liquids (PLALs) using single-element nanoparticles (e.g., Si, Au). The formed nanocomposites combined modalities of Si (paramagnetic defects) and Au (plasmonic features) showing narrow size distributions as compared to starting nanocrystals. Their size dispersions also revealed fluence-independent behaviour contrary to single-element nanoparticles. The laser ablation time-dependent concentration of colloidal solutions as well as their chemical stability was examined. Further perspectives of laser-synthesized multi-element nanoparticles for nanomedicine applications as carriers for drug delivery as well as a radionuclide (RN) containing diagnostic and therapeutic nanotools were proposed. These results will help in understanding the design of multi-component nanostructures using pulsed laser ablation and facilitate their synthesis for required applications.

2. Materials and Methods

To form single-component nanoparticles such as silicon (Si NPs) and gold (Au NPs), a method of direct pulsed laser ablation of a solid target immersed in deionized water was employed (Figure 1). The laser treatment was carried out using a picosecond laser (~6 ps pulse duration) at 1030 nm wavelength with a 10,000 Hz repetition rate. The laser beam was focused by a galvoscanner with a focal distance of 162 mm and moved at the $10 \times 10 \text{ mm}^2$ area with a velocity of 2 m/s. The liquid thickness was 3 mm, and the spot size was experimentally estimated as ~50 μm. The laser fluence was controlled by a λ/2 plate and was fixed at a 100 μJ/pulse value. In order to estimate the concentration of the prepared nanoparticles, the mass of the targets was measured before and after the laser treatment. Afterwards, multi-component nanostructures were formed via the same procedure using the previously obtained colloidal solutions (0.1 g/L concentration) prepared at 300 s laser ablation time. So, Si/Au NPs (Au/Si NPs) were prepared via the laser ablation of a gold (silicon) target immersed in Si NPs (Au NPs) colloidal solutions using the same experimental conditions (Figure 1). For some experiments, either laser fluence or ablation time were changed.

To estimate the size distribution of synthesized single- and multi-component NPs, a high-resolution transmission electron microscope (HR-TEM) was used. For this purpose, a small amount (5 μL) of freshly prepared NPs was dropped on a carbon-coated copper grid. The corresponding size distributions were calculated via the ImageJ software using more than 500 particles.

To find out the difference between the properties of single- and multi-component nanoparticles, several methods were used. Firstly, their absorbance was analysed (a cuvette with deionized water was used as a reference) using a Shimadzu UV-2600 spectrophotometer (Shimadzu Corporation, Kyoto, Japan) equipped with an integrating sphere (2 mm slit width and 2 s accumulation time). The Raman responses were investigated using a Horiba micro-Raman system equipped with a highly sensitive CCD camera and a laser with 532 nm wavelength (10 mW power and 2 s acquisition time). Paramagnetic defect states were examined with the help of a laboratory-built electron paramagnetic resonance

(EPR) spectrometer (~9.8 GHz, 5 G modulation amplitude, 100 kHz modulation frequency, 20 dB microwave power attenuation, and ~10^{10} spin/g sensitivity) [34,39].

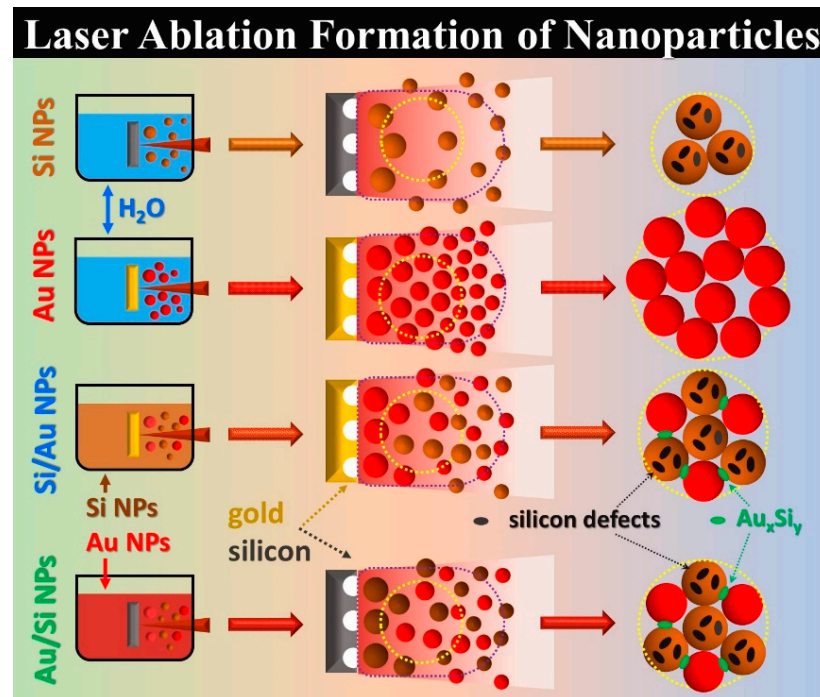**Figure 1.** Laser ablation in liquids synthesis of single- and multi-component nanoparticles.

3. Results and Discussion

To reveal changes in the optical properties of single- and multi-component nanoparticles during the synthesis, they were investigated using UV–Vis spectroscopy at different experimental conditions (Figure 2). Firstly, absorption coefficient spectra of Si NPs and Au NPs were analysed for a set of nanostructures prepared at different ablation times (30–600 s). These results provide an idea of how the absorbance is changed during continuous laser treatment, allowing the control of the plasmonic performance of nanocomposites. In all cases, one can state the increase in optical losses of nanostructures formed at a larger laser irradiation time can be associated with a higher nanoparticle concentration in this case. Indeed, as it is known, the concentration of a solution is directly connected with its absorbance following the relationship:

$$\mathbf{A} = \boldsymbol{\varepsilon} \cdot \mathbf{c} \cdot \mathbf{l} \tag{1}$$

Here, **A** is the solution absorbance, $\boldsymbol{\varepsilon}$ [M^{-1}·cm^{-1}] is its molar absorption coefficient, **c** [M] is its molar concentration, and **l** [cm] is an optical path length. Moreover, as it clearly follows in Figure 3, a larger ablation time provoked a higher concentration of single-element nanoparticles. Thus, evidently, the increase in the nanoparticle absorption is caused by their higher concentration in colloidal solutions. However, it is worth noticing that some changes in optical losses can also be associated with a modification of the size or chemical content of nanoparticles that occurred during prolonged laser treatment. Indeed, different processes can take place under laser irradiation, strongly depending on the molecular ambient of nanostructures. In particular, laser-induced fragmentation or agglomeration as well as a change in the oxidation state can occur in colloids influenced by properties of a liquid medium or its surroundings and will be studied in detail separately.
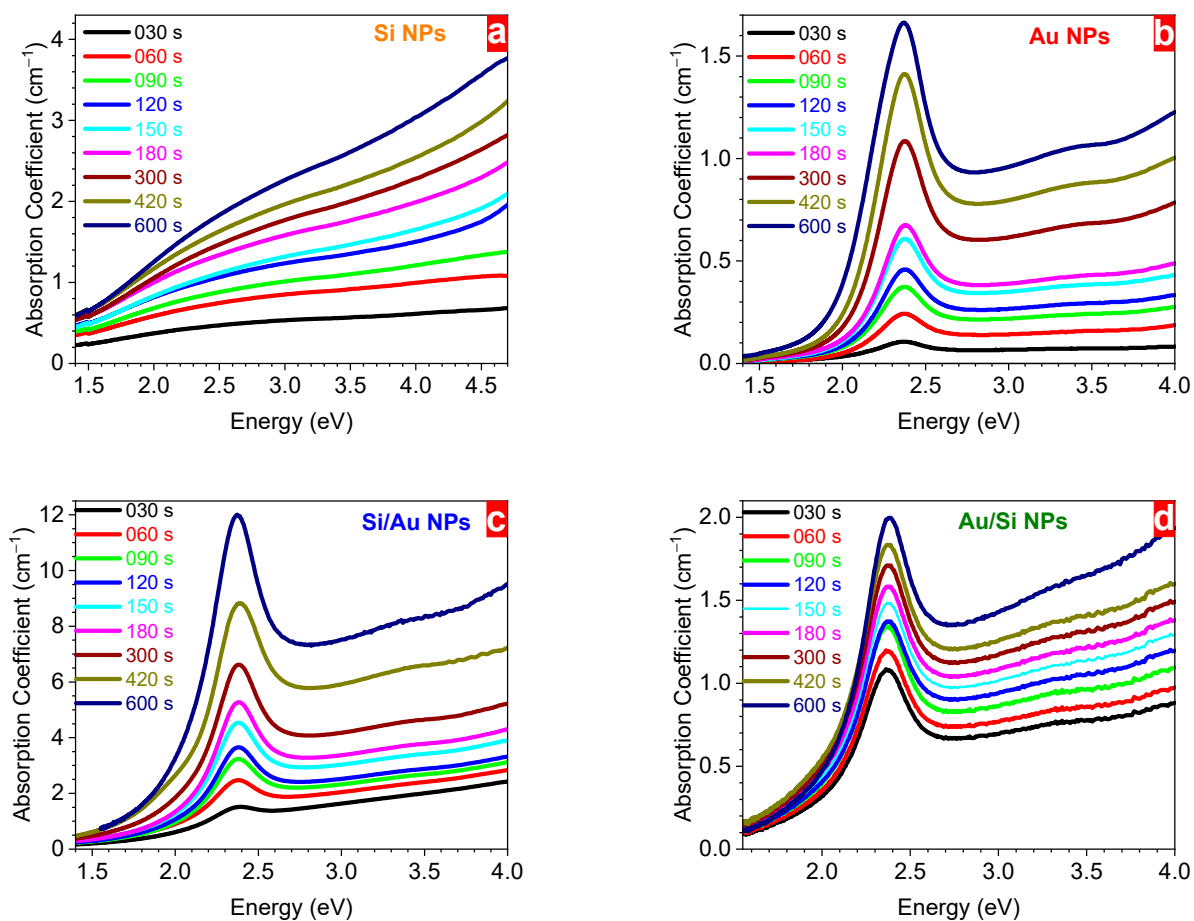
Figure 2. Absorption coefficient spectra of single- and multi-component nanoparticles: (**a**) Si NPs, (**b**) Au NPs, (**c**) Si/Au NPs, and (**d**) Au/Si NPs.
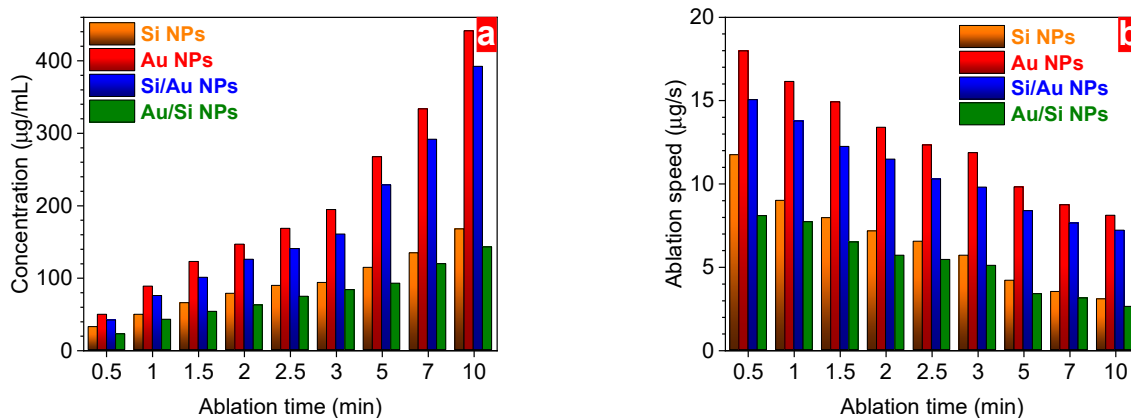

Figure 3. Ablation time dependences of (**a**) mass concentration and (**b**) ablation speed for single- and multi-component nanoparticles.

The formation of both Si/Au and Au/Si multi-component nanocomposites was agccompanied by a transformation of their absorbance spectra. In the first case, it was observed that the appearance of a plasmonic maximum at around 2.38 eV (521 nm) became stronger with the increase in the laser ablation time (Figure 2c). These modifications are associated with the increase in the gold content in nanocomposites provoked by prolonged laser ablation. A larger absorption coefficient of Si/Au NPs as compared to Au NPs is associated with a higher amount of plasmonic absorption centres. Indeed, laser ablation of the gold target in deionised water leads to the formation of pure Au NPs of large sizes. At the same time, in

the case of laser ablation in the presence of Si NPs, the latter can prevent the aggregation of gold nanoclusters from each other. Here, gold nanoclusters interact with laser-fragmented Si NPs creating a larger amount of composite nanostructures instead of forming of a smaller amount of larger Au NPs. Thus, the presence of Si NPs in deionized water can result in a larger number of Si/Au NPs with plasmonic properties in comparison with Au NPs. In the case of Au/Si nanocomposites formed from bare plasmonic nanoparticles, one can mention moderate changes in the efficiency of the plasmonic absorbance (Figure 2d). Here, laser ablation led to an increase in the silicon amount in the nanostructures that does not strongly affect plasmonic properties. Some increase in the absorbance intensity can be associated with the laser-induced fragmentation of nanoparticles decreasing their size [40]. It changes the amount of plasmonic nanoparticles in a solution providing a contribution to the optical spectra while their mass remains the same. However, in the case of Si/Au NPs, the mass of gold considerably increases with the laser ablation time. Moreover, this mass can be redistributed in a large amount of gold nanostructures due to the interaction with Si NPs as it was described above. Thus, the amount of plasmonic centres strongly increases with the ablation time in the case of Si/Au NPs, and one can easily control the efficiency of plasmonic properties of nanocomposites taking into account an approach used for the synthesis.

　　To define the number of nanostructures in colloidal solutions, their concentration and ablation speed were estimated using a gravimetric method. The mass concentration of both single- and bi-component nanoparticles showed a permanent increase with the ablation time (Figure 3a). These values were estimated as a mass difference of a corresponding target before and after laser ablation at a certain time. For composite nanoparticles, the mass difference indicated in Figure 3 was obtained at the second step (Au for Si/Au NPs and Si for Au/Si NPs), which is shown in Figure 3a. One can see that the mass concentration of pure Au NPs is larger than that of Si NPs, which can be associated with a higher density of gold (19.32 g/cm^3) as compared to that of silicon (2.33 g/cm^3). However, the relative difference of the concentrations is less than the ratio between their density values because of the possible following reasons. Firstly, density values are assigned for bulk materials while they can considerably differ for nanostructures formed at different synthesis conditions. Secondly, the laser-assisted synthesis in the aqueous medium can also change the chemical composition of nanostructures due to the oxidation process. Thirdly, silicon and gold nanostructures also possess different sizes of nanoparticles, in particular, showing a bimodal size distribution in the case of plasmonic ones [28,41]. Regarding the synthesis of composite nanocrystals (both Si/Au and Au/Si NPs), the experimental conditions changed. In these cases, the liquid contains NPs, which affect the concentration of nanocomposites due to the change in the optical properties of the system. These nanoparticles decrease the effective laser energy deposited on the surfaces due to their absorbance and scattering, resulting in a lower concentration of nanocomposites as compared to single-component ones (Si/Au NPs vs. Au NPs and Au/Si NPs vs. Si NPs). These differences in the concentration of NPs were also reflected in a corresponding ablation speed (Figure 3b). In all cases, the ablation speed had a tendency to decrease with the increasing duration of laser ablation (Figure 3b). It can be a consequence of considerable changes in the physico-chemical properties of colloidal solutions during the ultrafast laser treatment. In particular, it will result in higher optical losses (Figure 2) due to the increase in the concentration of NPs at a longer laser ablation time (Figure 3a). Hence, it can certainly provoke a strong decrease in the effective laser energy reaching the surface of the ablated targets. These experimental data can help with estimating the concentration of laser-synthesized single-element and composite nanoparticles and to find out appropriate experimental conditions for the synthesis.

　　To confirm the merging of various chemical elements due to the ultrafast laser treatment, energy-dispersive X-ray analysis was performed on both Si/Au and Au/Si NPs formed at 600 s laser ablation with mean size ~9 nm (Figure 4). For this purpose, a single composite nanoparticle isolated from other ones was investigated by TEM coupled with

an EDX spectrometer. One can see several maxima located at different energy positions associated with various transitions in different atoms. Copper peaks at around 1 keV, 8 keV, and 9 keV originated from used copper TEM grids (Figure 4). Other EDX responses corresponded to silicon (~1.7 eV) and gold (~2.1 eV and ~9.7 eV) in laser-synthesized composite nanoparticles. In the case of Si/Au NPs, the chemical content was estimated as follows: 64% of gold atoms and 36 % of silicon ones, while it was lower for Au/Si NPs at 51% of silicon and 49% of gold. Figure 4c depicts a phase diagram of Au-Si indicating the separation between liquid and solid phases of gold and silicon with the following melting points: 1064 °C (gold) and 1414 °C (silicon) [42]. A corresponding eutectic point is located at 363 °C for the Au-Si alloy with 19% silicon atoms, while Si/Au and Au/Si nanocomposites studied in this work have higher temperatures (Figure 4c). Such a discrepancy might occur due to a difference in the process of the formation of composite nanostructures. Indeed, in the first case, Si NPs were prepared in water during the first step of laser synthesis. However, Au/Si NPs were formed during the second step by ablating a silicon target immersed in water with the presence of Au NPs. Plasmonic nanoparticles influenced the conditions of the irradiation of a silicon wafer because of the shielding effects created by Au nanostructures. As a result, a lower amount of energy was deposited on the silicon's surface, leading to a lower amount of ablated silicon nanoclusters. More detailed studies of both types of composite nanoparticles formed at different ablation times will be investigated additionally via EDX, XPS, and XRD techniques in order to establish the nanoparticles' structure at different irradiation times. Thus, the aforementioned two-step laser treatment allows us to produce composite nanoparticles starting from colloidal solutions of bare semiconductor or plasmonic nanostructures.

To estimate the size distributions of nanoparticles, a transmission electron microscopy study was carried out and the obtained images were treated. It was found that all nanoparticles possessed a round shape with a significant difference in sizes between single- and multi-component nanostructures (Figure 5). Indeed, pure Si NPs and Au NPs revealed broad size dispersions of nanoparticles (FWHM > 20 nm) that were fitted using a Gaussian function (Figure 6). Moreover, plasmonic nanomaterials also consisted of two populations at ~19 nm and ~34 nm. It can point to different mechanisms of nanoparticle formation such as the decomposition of ablated species or their agglomeration in a cavitation bubble [40,41], while silicon ones show only one contribution at ~36 nm (Figure 6). Further modifications of the nanostructures using the laser ablation of targets immersed in these colloidal solutions significantly changed their size. Both types of composite silicon–gold nanoparticles demonstrated very narrow size distributions (FWHM ~ 5 nm) with much lower mean sizes (~8 ÷ 9 nm) (Figure 6). It is worth noticing that the size dispersion was similar for both Si/Au NPs and Au/Si NPs independent of the synthesis conditions. The found discrepancy in the size distributions as well as the similar behaviour of the size distributions in the case of nanocomposites demonstrate the significant difference between physico-chemical processes that occurred during the formation of single- and multi-component nanostructures.

To establish the influence of the laser energy on the dimension of the nanostructures, their mean sizes were estimated for these four types of nanoparticles formed at different laser fluences varied in the range of 50–175 μJ/pulse (Figure 7). Both multi-component nanostructures indicated fluence dependences different from single-component ones (Figure 7). Indeed, both Si/Au and Au/Si NPs possessed no dependences of their mean sizes (~8 nm) on the used laser fluence while their single-component counterparts showed a linear decrease from 47 nm to 24 nm (Si NPs) or increase from 9 nm to 30 nm (Au NPs) of the mean size with the increase in the laser fluence from 50 to 175 μJ/pulse. One can speculate that this behaviour can be associated with a considerable difference in the mass of these elements. Hence, silicon species formed due to laser ablation obtained higher kinetic energy than gold ones when absorbing the same amount of the laser energy. Thus, a cavitation bubble where the growth of nanoparticles takes place contains a higher amount of gold nanostructures than silicon ones, resulting in a larger size of Au NPs.
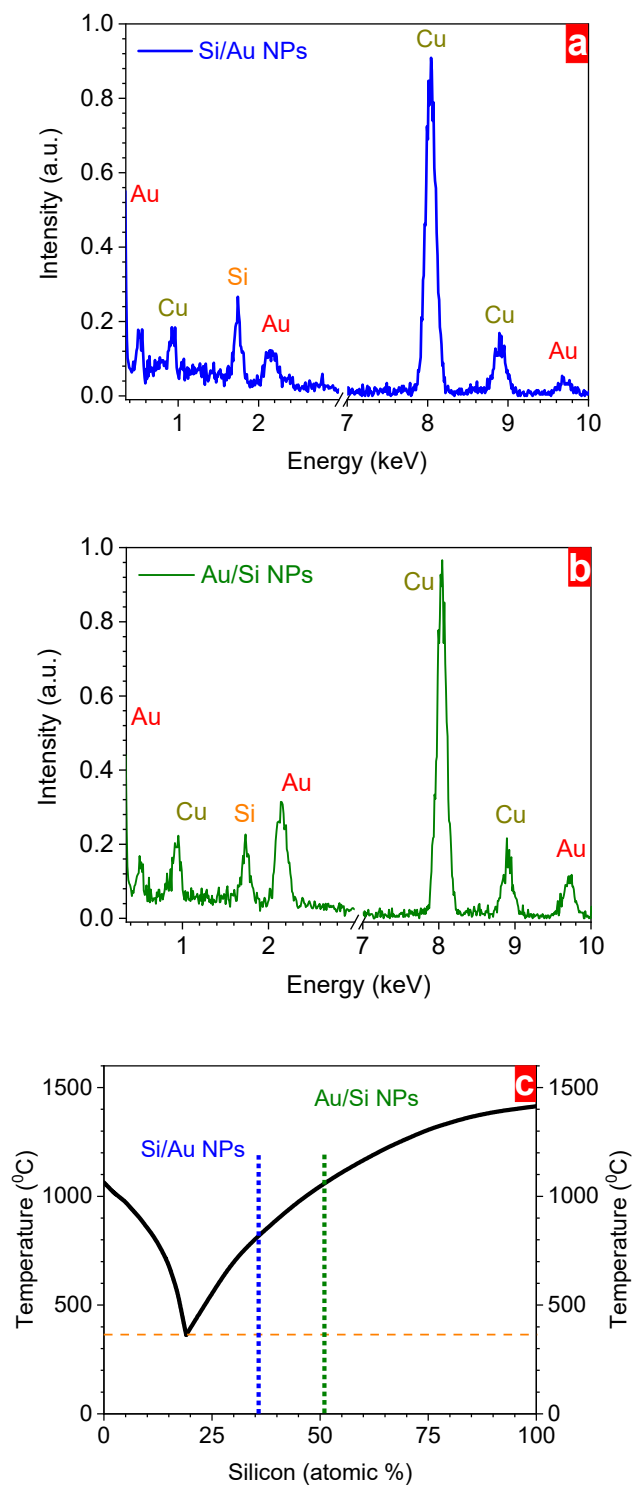
Figure 4. Energy-dispersive X-ray spectra of (**a**) Si/Au NPs and (**b**) Au/Si NPs formed at 600 s laser ablation time; (**c**) Au-Si phase diagram (a horizontal line at 363 °C is the eutectic point of the Au-Si alloy. Vertical lines correspond to the studied nanocomposites. Blue color was assigned for Si/Au NPs, green color—for Au/Si NPs, orange—for Si, red—for Au).
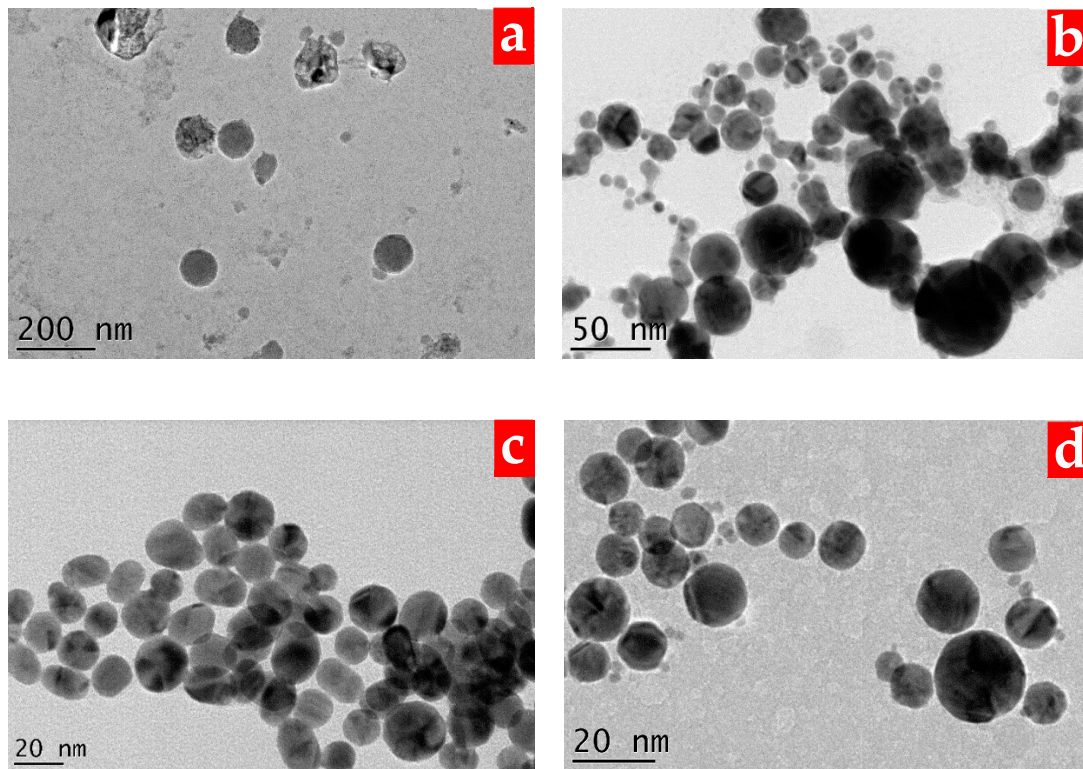
Figure 5. TEM images of single- and multi-component nanoparticles: (**a**) Si NPs, (**b**) Au NPs, (**c**) Si/Au NPs, and (**d**) Au/Si NPs.
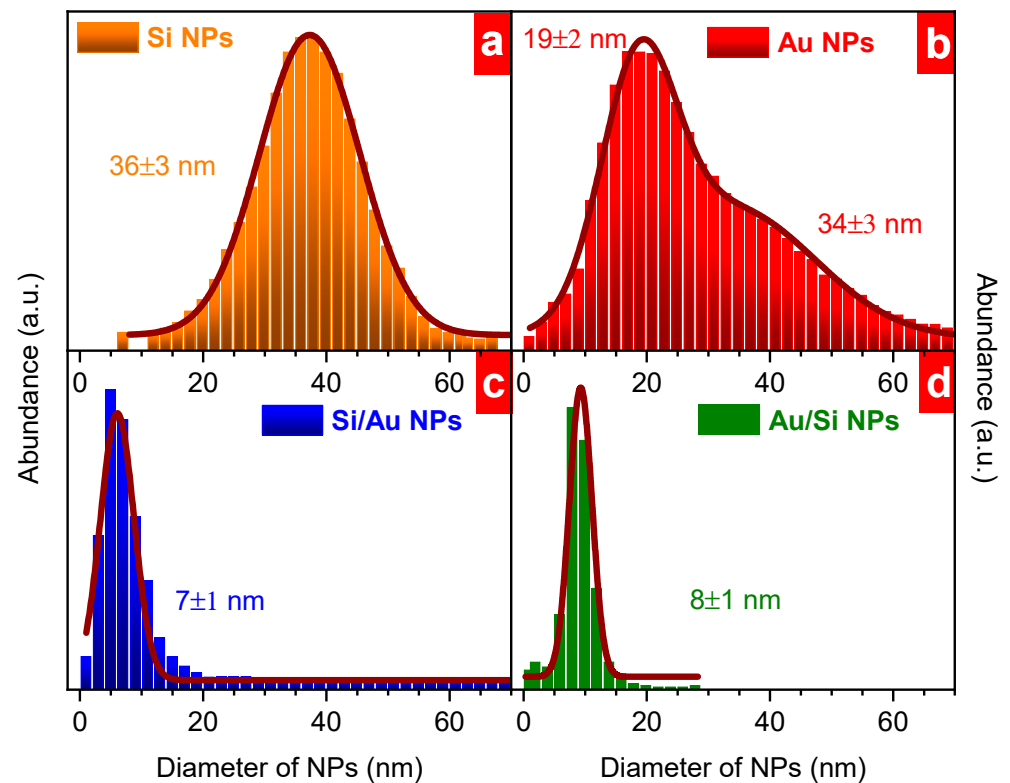

Figure 6. Size distributions of laser-synthesized single- ((**a**) Si NPs, (**b**) Au NPs) and multi-component ((**c**) Si/Au NPs, (**d**) Au/Si NPs) nanoparticles. Laser fluence is 100 μJ/pulse. The values indicate the mean diameter of the nanoparticles.
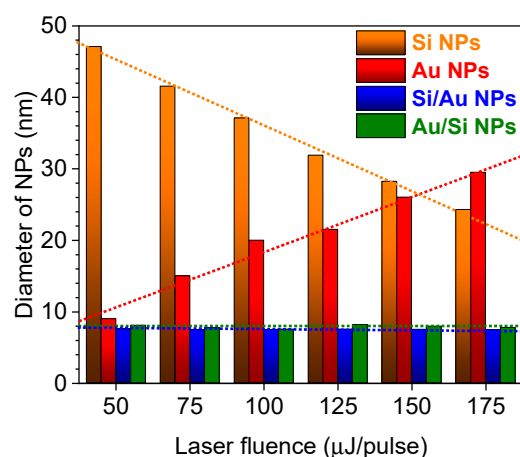
Figure 7. Laser fluence-dependent mean size of single- and multi-component nanoparticles estimated using TEM.

Nevertheless, the presence of both elements in the "reactor chamber" completely changes the picture. In this case, the situation can be quite similar for both Si/Au and Au/Si NPs. Indeed, in the first case, Si NPs can be decomposed during laser fragmentation while gold nanostructures are emitted from the gold target (and vice versa in the case of Au/Si NPs). However, the local concentration of nanostructures of each element can significantly differ due to the impact of several reasons significantly complicating the process of the nanocomposite synthesis and depending on deposited laser energy. For instance, the local concentration of nanoparticles in these cases as well as their sizes close to the laser spot focus can attenuate the deposited laser energy in different ways. Moreover, starting from the first seconds of the laser ablation, the absorption and scattering of the light will be permanently changed due to the decomposition of nanoparticles already dispersed in colloidal solutions, as well as due to the emission of new nanostructures. Thus, the size of nanoparticles and the extinction of the liquid will alter the synthesis conditions every time. However, the absence of any influences of such changes on the nanocomposite sizes can provide grounds to assume that mechanisms of the synthesis of multi-component nanoparticles significantly differ from single-component ones. One can speculate that physico-chemical processes occurring between silicon and gold elements play a significant role due to considerable local changes in the behaviour of different ablated species requiring a deeper study.

To establish the multi-functionality of laser-synthesized nanocomposites, their Raman and EPR spectra were investigated in comparison with Si NPs and Au NPs. It was found that only pure Si NPs exhibited clear Raman responses at ~520.4 cm^{-1} that can be assigned to the crystalline silicon phase in large NPs (Figure 8a). Using the following relationship between the Raman shift and the nanostructure size one can estimate an approximate mean size of silicon nanoparticles:

$$\Delta\upsilon = -52.3 \cdot (0.543/\mathbf{d})1.586 \tag{2}$$

where $\Delta\upsilon$ is a Raman spectral shift of the nanostructures of the size $\mathbf{d}$ in comparison with bulk silicon (520.5 cm^{-1}) [43]. Thus, this small Raman shift (~0.06 cm^{-1}) corresponds to the nanostructures with a size of ~40 nm, which is a close value to that estimated via TEM observations (Figure 6). It is worth noticing that no Raman responses were detected for all gold-containing nanostructures, which can indicate the large amount of gold on the NP surface irradiated with the visible light or amorphous structure of NPs. At the same time, EPR spectra of all silicon-based nanomaterials exhibited clear spectra that were similar in all cases (Figure 8b). The same spectra shape can point out any changes in the paramagnetic defect structure as a result of the laser treatment. Some changes in the concentration of paramagnetic defects (not studied in this research) can be due

to the modifications of the (i) chemical composition of multi-component nanostructures (e.g., silicon-gold bonding, nanoparticle concentration, oxidation state, etc.) or (ii) their sizes during the two-step laser treatment approach. It is worth noticing that this type of defect can be assigned to unpaired electrons in disordered silicon [44]. The detection of the amorphous silicon in this case, together with the absence of any Raman silicon responses, can imagine a core@shell Au@Si structure where core Si exhibits a clear EPR signal insensitive to the visible irradiation. In order to establish the exact structures of both Si/Au and Au/Si nanoparticles, a comprehensive study using HR-TEM, EDX, XPS, and XRD techniques will be performed separately. These results demonstrate the possibility of using composite nanoparticles for non-invasive tracking using different kinds of magnetic resonance technologies.
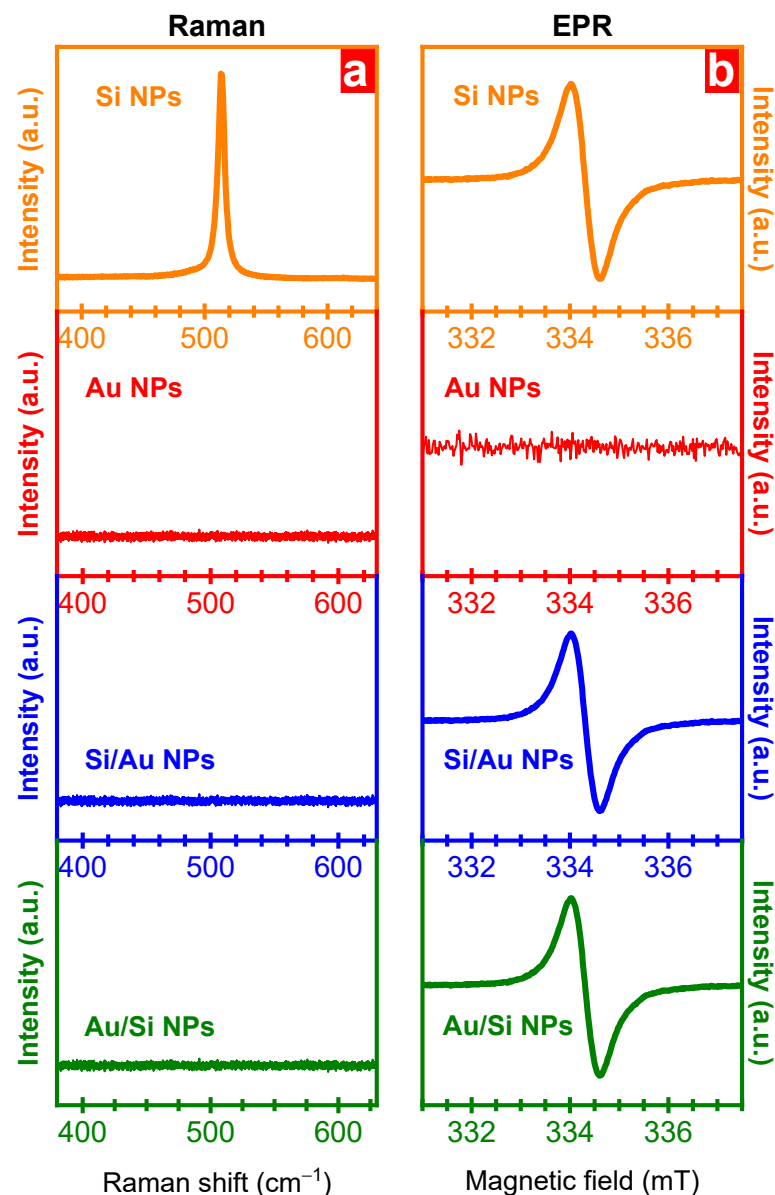

Figure 8. (**a**) Raman and (**b**) EPR spectra of single- and multi-component nanoparticles. Laser fluence is 100 μJ/pulse.

The approaches presented in this work for the formation of chemically ultrapure bi-component plasmonic nanocomposites can be promising for the field of catalysis or biomedicine with the aim of creating a multi-functional nanotool. Firstly, it is a facile way to incorporate elements with required modalities in already-existing nanoparticles using

high chemical purity conditions. It can extend their applications in catalysis, bio-, magnetic or electrical applications [36,45–48], allowing them to achieve different aims at the same time, using only one type of nanomaterial. Another point can be related to the development of nanoparticle-based carriers of radionuclides (RNs) for biomedical applications. Until now, they were usually prepared via different complex methods and successfully assessed for different theranostic applications including cancer therapy [49–53]. The aforementioned laser-based technology can be a new promising approach used for the development and easy synthesis of nanoparticle radiocarriers in chemically pure conditions. In this case, a complex nanoplatform merging not only semiconductor and plasmonic/magnetic elements but also different types of RNs can be designed for different directions of the life science field (Figure 9). In particular, "key" nanoparticles that are necessary for theranostic applications can be treated in the presence of different elements, adding new "radio" modalities whose efficiency can be controlled by the treatment time. This technique can considerably simplify the formation of novel types of radiopharmaceuticals with an individually controlled performance.
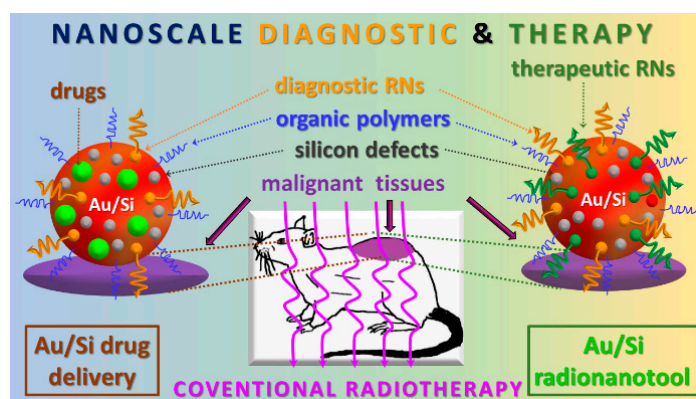

Figure 9. Perspectives of laser-synthesized multi-component nanoparticles for diagnostic and therapeutic purposes.

4. Conclusions

In summary, composite nanoparticles are formed via ultrafast laser ablation using either semiconductor or plasmonic nanostructures as starting materials. In both cases, the combination of silicon and gold elements is observed, accompanied by a significant narrowing of the size distribution. This merging leads to the disappearance of the Raman signal attributed to crystalline silicon while unpaired electrons of the silicon paramagnetic defects are detectable. The changing of the laser fluence does not modify the mean sizes of both types of silicon–gold nanocomposites contrary to single-element counterparts. Laser ablation time affects the concentration of synthesized nanoparticles as well as the ablation speed. The variation of the laser ablation time provokes smooth modifications of the absorbance properties of composite nanostructures, allowing the adjustment of their efficiency to differ depending on a started material. The extension of the laser ablation approach for easy synthesizing of radiolabelled nanoparticles with controlled performance is proposed.

Conflicts of Interest: The authors declare no conflict of interest.

References

1. Peng, K.-Q.; Wang, X.; Wu, X.-L.; Lee, S.-T. Platinum Nanoparticle Decorated Silicon Nanowires for Efficient Solar Energy Conversion. *Nano Lett.* **2009**, *9*, 3704–3709. [CrossRef] [PubMed]
2. Zhu, J.; Yu, Z.; Burkhard, G.F.; Hsu, C.-M.; Connor, S.T.; Xu, Y.; Wang, Q.; McGehee, M.; Fan, S.; Cui, Y. Optical Absorption Enhancement in Amorphous Silicon Nanowire and Nanocone Arrays. *Nano Lett.* **2009**, *9*, 279–282. [CrossRef] [PubMed]
3. Pathak, N.K.; Chander, N.; Komarala, V.K.; Sharma, R.P. Plasmonic Perovskite Solar Cells Utilizing Au@SiO$_2$ Core-Shell Nanoparticles. *Plasmonics* **2017**, *12*, 237–244. [CrossRef]
4. Ryabchikov, Y.V.; Lysenko, V.; Nychyporuk, T. Enhanced Thermal Sensitivity of Silicon Nanoparticles Embedded in (nano-Ag)/SiN$_x$ for Luminescent Thermometry. *J. Phys. Chem. C* **2014**, *118*, 12515–12519. [CrossRef]
5. Ryabchikov, Y.V.; Alekseev, S.A.; Lysenko, V.; Bremond, G.; Bluet, J.-M. Photoluminescence thermometry with alkyl-terminated silicon nanoparticles dispersed in low-polar liquids. *Phys. Status Solidi-R* **2013**, *7*, 414–417. [CrossRef]
6. Ryabchikov, Y.V.; Alekseev, S.A.; Lysenko, V.; Bremond, G.; Bluet, J.-M. Photoluminescence of silicon nanoparticles chemically modified by alkyl groups and dispersed in low-polar liquids. *J. Nanopart. Res.* **2013**, *15*, 1535. [CrossRef]
7. Cui, Y.; Lieber, C.M. Functional Nanoscale Electronic Devices Assembled Using Silicon Nanowire Building Blocks. *Science* **2001**, *2915*, 851–853. [CrossRef]
8. Chen, L.J. Silicon nanowires: The key building block for future electronic devices. *J. Mater. Chem.* **2007**, *17*, 4639–4643. [CrossRef]
9. Ryabchikov, Y.V.; Belogorokhov, I.A.; Vorontsov, A.S.; Osminkina, L.A.; Timoshenko, V.Y.; Kashkarov, P.K. Dependence of the Singlet Oxygen Photosensitization Efficiency on Morphology of Porous Silicon. *Phys. Status Solidi A* **2007**, *204*, 1271–1275. [CrossRef]
10. Konstantinova, E.A.; Demin, V.A.; Vorontzov, A.S.; Ryabchikov, Y.V.; Belogorokhov, I.A.; Osminkina, L.A.; Forsh, P.A.; Kashkarov, P.K.; Timoshenko, V.Y. Electron Paramagnetic Resonance and Photoluminescence Study of Si Nanocrystals—Photosensitizers of Singlet Oxygen Molecules. *J. Non-Cryst. Solids* **2006**, *352*, 1156–1159. [CrossRef]
11. Ryabchikov, Y.V.; Belogorokhov, I.A.; Gongalskiy, M.B.; Osminkina, L.A.; Timoshenko, V.Y. Photosensitized Generation of Singlet Oxygen in Powders and Aqueous Suspensions of Silicon Nanocrystals. *Semiconductors* **2011**, *45*, 1059–1063. [CrossRef]
12. Tu, C.-C.; Awasthi, K.; Chen, K.-P.; Lin, C.-H.; Hamada, M.; Ohta, N.; Li, Y.-K. Time-gated Imaging on Live Cancer Cells Using Silicon Quantum Dot Nanoparticles with Long-lived Fluorescence. *ACS Photonics* **2017**, *4*, 1306–1315. [CrossRef]
13. Kharin, A.Y.; Lysenko, V.V.; Rogov, A.; Ryabchikov, Y.V.; Geloen, A.; Tishchenko, I.; Marty, O.; Sennikov, P.G.; Kornev, R.A.; Zavestovskaya, I.N.; et al. Bi-modal nonlinear optical contrast from Si nanoparticles for cancer theranostics. *Adv. Opt. Mater.* **2019**, *7*, 1801728. [CrossRef]
14. Tollemeto, M.; Huang, Z.; Christensen, J.B.; Nielsen, H.M.; Rønholt, S. Mucoadhesive Dendrons Conjugated to Mesoporous Silica Nanoparticles as a Drug Delivery Approach for Orally Administered Biopharmaceuticals. *ACS Appl. Mater. Interfaces* **2023**, *15*, 8798–8810. [CrossRef] [PubMed]
15. Fathy, M.M.; Yassin, F.M.; Elshemey, W.M.; Fahmy, H.M. Insight on the Dependence of the Drug Delivery Applications of Mesoporous Silica Nanoparticles on Their Physical Properties. *Silicon* **2023**, *15*, 61–70. [CrossRef]
16. Ahmed, H.; Gomte, S.S.; Prathyusha, E.; Prabakaran, A.; Agrawal, M.; Alexander, A. Biomedical applications of mesoporous silica nanoparticles as a drug delivery carrier. *J. Drug Deliv. Sci. Technol.* **2022**, *76*, 103729. [CrossRef]
17. Karthikeyan, L.; Sobhana, S.; Yasothamani, V.; Gowsalya, K.; Vivek, R. Multifunctional theranostic nanomedicines for cancer treatment: Recent progress and challenges. *Biomed. Eng. Adv.* **2023**, *5*, 100082. [CrossRef]
18. Jiang, W.; Low, B.Q.L.; Long, R.; Low, J.; Loh, H.; Tang, K.Y.; Chai, C.H.T.; Zhu, H.; Zhu, H.; Li, Z.; et al. Active Site Engineering on Plasmonic Nanostructures for Efficient Photocatalysis. *ACS Nano* **2023**, *17*, 4193–4229. [CrossRef] [PubMed]
19. Verma, P.; Kuwahara, Y.; Mori, K.; Raja, R.; Yamashita, H. New insights in establishing the structure-property relations of novel plasmonic nanostructures for clean energy applications. *EnergyChem* **2022**, *4*, 100070. [CrossRef]
20. Mitra, S.; Mitali, M. Diverse bio-sensing and therapeutic applications of plasmon enhanced nanostructures. *Mater. Today* **2022**, *57*, 225–261. [CrossRef]
21. Nowak-Jary, J.; Machnicka, B. Pharmacokinetics of magnetic iron oxide nanoparticles for medical applications. *J. Nanobiotechnol.* **2022**, *20*, 305. [CrossRef]
22. Naghdi, M.; Ghovvati, M.; Rabiee, N.; Ahmadi, S.; Abbariki, N.; Sojdeh, S.; Ojaghi, A.; Bagherzadeh, M.; Akhavan, O.; Sharifi, E.; et al. Magnetic nanocomposites for biomedical applications. *Adv. Colloid Interface Sci.* **2022**, *308*, 102771. [CrossRef]
23. Laha, S.S.; Thorat, N.D.; Singh, G.; Sathish, C.I.; Yi, J.; Dixit, A.; Vinu, A. Rare-Earth Doped Iron Oxide Nanostructures for Cancer Theranostics: Magnetic Hyperthermia and Magnetic Resonance Imaging. *Small* **2022**, *18*, 2104855. [CrossRef]
24. Falzarano, M.S.; Flesia, C.; Cavalli, R.; Guiot, C.; Ferlini, A. Nanodiagnostics and Nanodelivery Applications in Genetic Alterations. *Curr. Pharm. Des.* **2018**, *24*, 1717–1726. [CrossRef]
25. Li, J.; Liu, J.; Chen, C. Remote Control and Modulation of Cellular Events by Plasmonic Gold Nanoparticles: Implications and Opportunities for Biomedical Applications. *ACS Nano* **2017**, *11*, 2403–2409. [CrossRef]
26. Iqbal, M.Z.; Ren, W.; Saeed, M.; Chen, T.; Ma, X.; Yu, X.; Zhang, J.; Zhang, L.; Li, A.; Wu, A. A facile fabrication route for binary transition metal oxide-based Janus nanoparticles for cancer theranostic applications. *Nano Res.* **2018**, *11*, 5735–5750. [CrossRef]

27. Ma, J.; Lee, S.M.-Y.; Yi, C.; Li, C.-W. Controllable synthesis of functional nanoparticles by microfluidic platforms for biomedical applications—A review. *Lab. Chip* **2017**, *17*, 209–226. [CrossRef] [PubMed]

28. Ryabchikov, Y.V. Size Modification of Optically Active Contamination-Free Silicon Nanoparticles with Paramagnetic Defects by Their Fast Synthesis and Dissolution. *Phys. Status Solidi A* **2019**, *216*, A1800685. [CrossRef]

29. Kirillin, M.Y.; Sergeeva, E.A.; Agrba, P.D.; Krainov, A.D.; Ezhov, A.A.; Shuleiko, D.V.; Kashkarov, P.K.; Zabotnov, S.V. Laser-ablated silicon nanoparticles: Optical properties and perspectives in optical coherence tomography. *Laser Phys.* **2015**, *25*, 075604. [CrossRef]

30. Radičić, R.; Maletić, D.; Blažeka, D.; Car, J.; Krstulović, N. Synthesis of Silver, Gold, and Platinum Doped Zinc Oxide Nanoparticles by Pulsed Laser Ablation in Water. *Nanomaterials* **2022**, *12*, 3484. [CrossRef]

31. Pini, F.; Pilot, R.; Ischia, G.; Agnoli, S.; Amendola, V. Au–Ag Alloy Nanocorals with Optimal Broadband Absorption for Sunlight-Driven Thermoplasmonic Applications. *ACS Appl. Mater. Interfaces* **2022**, *14*, 28924–28935. [CrossRef]

32. Doñate-Buendia, C.; Spellauge, M.; Streubel, R.; Riahi, F.; Barcikowski, S.; Huber, H.P.; Gökce, B. Double-pulse laser ablation in liquids: Nanoparticle bimodality reduction by sub-nanosecond interpulse delay optimization. *J. Phys. D Appl. Phys.* **2023**, *56*, 104001. [CrossRef]

33. Verma, A.K.; Soni, R.K. Laser ablation synthesis of bimetallic gold-palladium core@shell nanoparticles for trace detection of explosives. *Opt. Laser Technol.* **2023**, *163*, 109429. [CrossRef]

34. Ryabchikov, Y.V. Facile Laser Synthesis of Multimodal Composite Silicon/Gold Nanoparticles with Variable Chemical Composition. *J. Nanopart. Res.* **2019**, *21*, 85. [CrossRef]

35. Ryabchikov, Y.V.; Behrends, J. Expedient Paramagnetic Properties of Surfactant-Free Plasmonic Silicon-Based Nanoparticles. *Opt. Quant. Electron.* **2020**, *52*, 177. [CrossRef]

36. Nasiri, P.; Doranian, D.; Sari, A.H. Synthesis of Au/Si nanocomposite using laser ablation method. *Opt. Laser Technol.* **2019**, *113*, 217–224. [CrossRef]

37. Gurbatov, S.O.; Puzikov, V.; Storozhenko, D.; Modin, E.; Mitsai, E.; Cherepakhin, A.; Shevlyagin, A.; Gerasimenko, A.V.; Kulinich, S.A.; Kuchmizhak, A.A. Multigram-Scale Production of Hybrid Au-Si Nanomaterial by Laser Ablation in Liquid (LAL) for Temperature-Feedback Optical Nanosensing, Light-to-Heat Conversion, and Anticounterfeit Labeling. *ACS Appl. Mater. Interfaces* **2023**, *15*, 3336–3347. [CrossRef]

38. Abbas, Z.A.; Khashan, K.S.; Hussain, Z.T. Silver (Ag) doped cadmium oxide (CdO) nanoparticles were synthesized through laser ablation in liquid for the sensing applications. *Opt. Quant. Electron.* **2023**, *55*, 587. [CrossRef]

39. Kulikov, I.; Panjwani, N.A.; Vereshchagin, A.A.; Spallek, D.; Lukianov, D.A.; Alekseeva, E.V.; Levin, O.V.; Behrends, J. Spins at work: Probing charging and discharging of organic radical batteries by electron paramagnetic resonance spectroscopy. *Energy Environ. Sci.* **2022**, *15*, 3275–3290. [CrossRef]

40. Maximova, K.; Aristov, A.; Sentis, M.; Kabashin, A.V. Size-controllable synthesis of bare gold nanoparticles by femtosecond laser fragmentation in water. *Nanotechnology* **2015**, *26*, 065601. [CrossRef] [PubMed]

41. Flimelova, M.; Ryabchikov, Y.V.; Behrends, J.; Bulgakova, N.M. Environmentally Friendly Improvement of Plasmonic Nanostructure Functionality towards Magnetic Resonance Applications. *Nanomaterials* **2023**, *13*, 764. [CrossRef] [PubMed]

42. Lin, J.-S.; Chen, C.-C.; Diau, W.W.-G.; Liu, T.-F. Fabrication and characterization of eutectic gold–silicon (Au–Si) nanowires. *J. Mater. Process. Technol.* **2008**, *206*, 425–430. [CrossRef]

43. Abderrafi, K.; Calzada, R.G.; Gongalsky, M.B.; Suarez, I.; Abarques, R.; Chirvony, V.S.; Timoshenko, V.Y.; Ibanez, R.; Martínez-Pastor, J.P. Silicon Nanocrystals Produced by Nanosecond Laser Ablation in an Organic Liquid. *J. Phys. Chem. C* **2011**, *115*, 5147–5151. [CrossRef]

44. Shimasaki, M.; Show, Y.; Iwase, M.; Izumi, T.; Ichinohe, T.; Nozaki, S.; Morisaki, H. Correlation between light emission and dangling bonds in porous silicon. *Appl. Surf. Sci.* **1996**, *92*, 617–620. [CrossRef]

45. Pan, S.; Wang, T.; Jin, K.; Cai, X. Understanding and designing metal matrix nanocomposites with high electrical conductivity: A review. *J. Mater. Sci.* **2022**, *57*, 6487–6523. [CrossRef]

46. Yuan, J.; Yao, G.; Pan, S.; Murali, N.; Li, X. Size Control of In Situ Synthesized TiB_2 Particles in Molten Aluminum. *Metall. Mater. Trans. A* **2021**, *52*, 2657–2666. [CrossRef]

47. Havelka, O.; Yalcinkaya, F.; Wacławek, S.; Padil, V.V.T.; Amendola, V.; Černíka, M.; Torres-Mendieta, R. Sustainable and scalable development of PVDF-OH Ag/TiOx nanocomposites for simultaneous oil/water separation and pollutant degradation. *Environ. Sci. Nano* **2023**. [CrossRef]

48. Scaramuzza, S.; Faria, C.M.G.; Coviello, V.; Forrer, D.; Artiglia, L.; Badocco, D.; Pastore, P.; Ghigna, P.; Postuma, I.; Cansolino, L.; et al. A Laser Synthesis Route to Boron-Doped Gold Nanoparticles Designed for X-Ray Radiotherapy and Boron Neutron Capture Therapy Assisted by CT Imaging. *Adv. Funct. Mater.* **2023**, 2303366. [CrossRef]

49. Chen, F.; Wang, M.; Du, Z.; Pu, Z.; Zhu, B. [31]I labeled pH-responsive gold nanoparticles for bimodal tumor diagnosis. *Mater. Lett.* **2023**, *330*, 133202. [CrossRef]

50. Ünak, P.; Yasakçı, V.; Tutun, E.; Karatay, K.B.; Walczak, R.; Wawrowicz, K.; Żelechowska-Matysiak, K.; Majkowska-Pilip, A.; Bilewicz, A. Multimodal Radiobioconjugates of Magnetic Nanoparticles Labeled with [44]Sc and [47]Sc for Theranostic Application. *Pharmaceutics* **2023**, *15*, 850. [CrossRef] [PubMed]

51. Petriev, V.M.; Tischenko, V.K.; Mikhailovskaya, A.A.; Popov, A.A.; Tselikov, G.; Zelepukin, I.; Deyev, S.M.; Kaprin, A.D.; Ivanov, S.; Timoshenko, V.Y.; et al. Nuclear nanomedicine using Si nanoparticles as safe and effective carriers of [188]Re radionuclide for cancer therapy. *Sci. Rep.-UK* **2019**, *9*, 2017. [CrossRef] [PubMed]

52. Türkkanı, G.; Güngör, B.; Cetin, O.; İçhedef, C.; Parlak, Y.; Gümüşer, F.G.; Bilgin, B.E.S.; Teksöz, S. Synthesis, radiolabeling and in vitro evaluation of azathioprine loaded magnetic solid lipid nanoparticles. *J. Radioanal. Nucl. Chem.* **2023**. [CrossRef]

53. Goel, M.; Mackeyev, Y.; Krishnan, S. Radiolabeled nanomaterial for cancer diagnostics and therapeutics: Principles and concepts. *Cancer Nano.* **2023**, *14*, 15. [CrossRef] [PubMed]